# Enhanced Thermoelectric Power in Dual-Gated Bilayer Graphene

Chang-Ran Wang,[1] Wen-Sen Lu,[1,2] Lei Hao,[1] Wei-Li Lee,[1,*] Ting-Kuo Lee,[1,2] Feng Lin,[3]
I-Chun Cheng,[3] and Jian-Zhang Chen[4]
[1]*Institute of Physics, Academia Sinica, Nankang, Taipei, Taiwan*
[2]*Department of Physics, National Taiwan University, Taipei, Taiwan*
[3]*Department of Electrical Engineering and Graduate Institute of Photonics and Optoelectronics,*
*National Taiwan University, Taipei, Taiwan*
[4]*Institute of Applied Mechanics, National Taiwan University, Taipei, Taiwan*
(Received 22 April 2011; published 26 October 2011)

The thermoelectric power of a material, typically governed by its band structure and carrier density, can be varied by chemical doping that is often restricted by solubility of the dopant. Materials showing large thermoelectric power are useful for many industrial applications, such as the heat-to-electricity conversion and the thermoelectric cooling device. Here we show a full electric-field tuning of thermoelectric power in a dual-gated bilayer graphene device resulting from the opening of a band gap by applying a perpendicular electric field on bilayer graphene. We uncover a large enhancement in thermoelectric power at a low temperature, which may open up a new possibility in low temperature thermoelectric application using graphene-based device.

DOI: 10.1103/PhysRevLett.107.186602 PACS numbers: 72.80.Vp, 72.15.Jf, 65.80.Ck, 73.63.Bd

Bilayer graphene (BLG) comprises two monolayers of graphene stacked as in bulk graphite exhibiting unusual massive chiral fermionic excitations [1–3]. Its conduction band and valence band touch at a charge neutral point (CNP) resembling a zero-gap semiconductor with an effective mass $m^* \approx 0.054 m_e$. Many interests reside on the band gap engineering in BLG by breaking its inversion symmetry, which is of particular importance for semiconductor device application. Ohta *et al.* [4] demonstrated the band gap opening by chemical doping of potassium onto the upper layer of a BLG placed on a silicon carbide substrate using angle-resolved photoemission spectroscopy. Soon later, Castro *et al.* [5] showed the band gap tuning by electric-field effect in a BLG device on a $SiO_2$(300 nm)/Si substrate with $NH_3$ adsorption on the upper layer to further enhance the layer asymmetry. More recently, a dual-gated geometry for band gap engineering was realized in BLG devices [6–9], where a BLG was sandwiched by a top gate and a bottom gate providing full electric-field control over its band structure.

In this Letter, we utilize high quality microcrystals of hexagonal boron nitride (hBN) as a top-gate dielectric, which was shown to impose less trapped charges and strain on graphene [10]. The dual-gated BLG devices we fabricated [11] show carrier mobility ($\sim$ 2000–3000 $\text{cm}^2/\text{V sec}$) comparable to the ones without a top gate (hBN). We demonstrate a full electric-field tuning of thermoelectric power (TEP) in bilayer graphene devices, which has been predicted theoretically [12] and originates from the opening of a band gap via the application of an out-of-plane electrical displacement field $\vec{D}$. We uncover an enhancement in TEP due to $\vec{D}$, which grows larger at lower temperatures attaining a value comparable to or exceeding those of $Bi_2Te_3$-based alloys and sodium cobaltates $Na_xCoO_2$ at similar $T$. Our result reveals the potential thermoelectric application using a graphene-based device.

The device geometry, which comprises a heater, two local thermometers (Rt1 and Rt2), three voltages leads, and a local top gate as shown in Fig. 1(a), enables the 4-probe measurements of resistance and TEP [11,13,14]. The thickness of the hBN microcrystal for this particular device is $\simeq 40$ nm determined by an atomic force microscope. We note that the top-gate effective region, shown as the shaded area in Fig. 1(a), only partially covers the BLG area between voltage leads. Therefore, an additional geometric factor needs to be considered in order to extract the sheet resistance and TEP for BLG under the top-gate effective region [11]. For the following discussion, we used the suffix $e$(ne) referring to the top-gate (non)effective region and suffix $\square$ for the sheet resistance.

Figure 1(b) shows a contour plot for the measured resistance $R$ at 200 K for the device shown in Fig. 1(a). The bottom-gate voltage $V_{\text{bg}}$ is swept up to $\pm 70$ V, while the top-gate voltage $V_{\text{tg}}$ is kept at a certain value from $-10$ to 10 V. The high $R$ states occur in regions with large $V_{\text{bg}}$ and $V_{\text{tg}}$ at opposite polarity defined in Fig. 1(a). When plotting ($V_{\text{tg}}$, $V_{\text{bg}}$) for the peak position of $R$ [Fig. 1(d)], it is nearly $T$ independent and shows excellent linearity giving a slope $\alpha \equiv dV_{\text{bg}}/dV_{\text{tg}} = -(\epsilon_t d_b)/(\epsilon_b d_t) \simeq -7.72$, where $\epsilon_{b(t)}$ and $d_{b(t)}$ refer to the relative bottom (top)-gate dielectric constant and bottom(top)-gate dielectric thickness, respectively [Fig. 1(c)]. Using $\varepsilon_b = 3.9(SiO_2)$ and $(d_b, d_t) = (300\text{ nm}, 40\text{ nm})$, we obtained a relative dielectric constant for hBN $\varepsilon_t \simeq 4.0$ in good agreement with the reported value for bulk hBN [10]. The

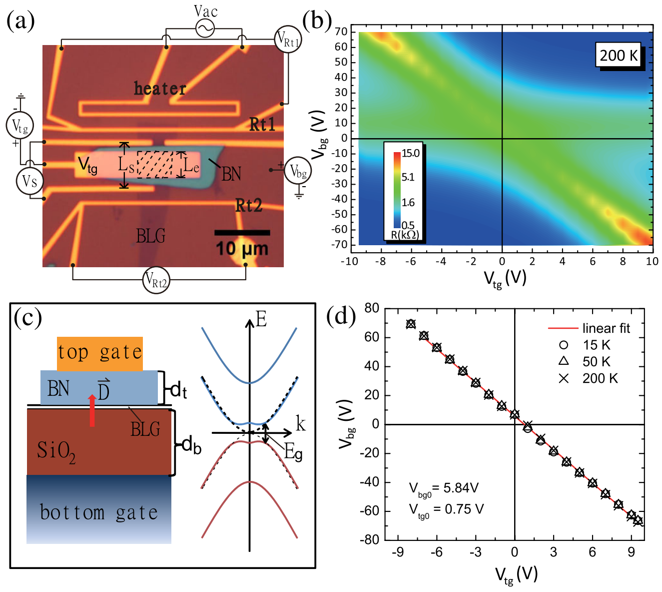

FIG. 1 (color online). (a) An optical image of a dual-gated BLG device with the shaded area referring to the top-gate effective region. The measurement setup is illustrated with labels in the figure and polarity definitions for $V_{tg}$ and $V_{bg}$. (b) A contour plot for the resistance (log scale) as a function of $V_{tg}$ and $V_{bg}$ at 200 K. The left panel of (c) illustrates the application of displacement field $\vec{D}$ on BLG using dual-gated geometry (not to scale). The right panel of (c) shows the band gap ($E_g$) opening due to the inversion symmetry breaking by $\vec{D}$. (d) The ($V_{tg}$, $V_{bg}$) values for resistance peaks in (b) at 15, 50, and 200 K. The linear fit shown as a red line gives $V_{bg0} = 5.84$ V and $V_{tg} = 0.75$ V.

introduction of $V_{bg}$ and $V_{tg}$ capacitively changes the carrier density in BLG and hence shifts its chemical potential ($\mu$). For a given $V_{tg}$, $R$ attains a peak value whenever $\mu$ is shifted back to the CNP by tuning $V_{bg}$ while giving a finite $\vec{D}$ on BLG that grows in magnitude with $V_{tg}$. The total unscreened displacement field $\vec{D}$ on BLG can be calculated by using $\vec{D} = [\varepsilon_b(V_{bg} - V_{bg0})/d_b - \varepsilon_t(V_{tg} - V_{tg0})/d_t]/2$, where $V_{bg0}$ and $V_{tg0}$ equal 5.84 and 0.75 V, respectively,

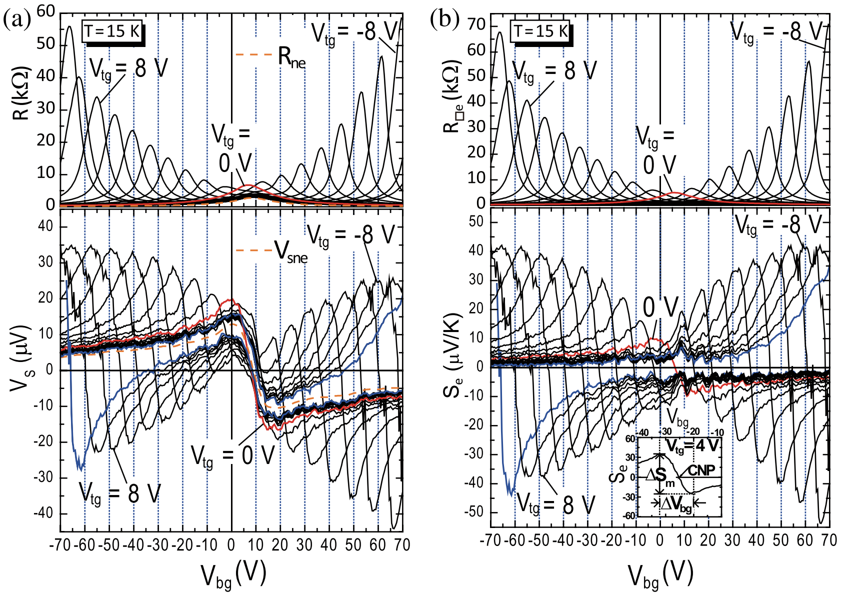

FIG. 2 (color online). The upper panel in (a) shows $R$ vs $V_{bg}$ for the dual-gated BLG at $T = 15$ K and different $V_{tg}$ values ranging from $-10$ to 10 V. The lower panel plots the corresponding thermoelectric signal $V_s$ at the same $T$. The dashed orange line represents the signal contribution from the top-gate noneffective region extracted from the blue curves with $V_{tg} = \pm 10$ V. (b) $V_{bg}$ dependence of extracted sheet resistance $R_{\square e}$ (upper panel) and TEP $S_e$ (lower panel) for the top-gate effective region. The thick red lines are the signals at $V_{tg} = 0$. The definitions for $\Delta S_m$ and $\Delta V_{bg}$ are shown in the inset of the lower panel using the $S_e - V_{bg}$ curve at $V_{tg} = +4$ V as an example.

determined from the linear fit shown in Fig. 1(d). Therefore, the large increase in the resistance peak is a direct consequence of the band gap opening [right panel in Fig. 1(c)] due to the inversion symmetry breaking by $\vec{D}$, which appears to be most dramatic in BLG [8].

At $V_{\rm tg} = 0$ and 15 K, $R$ attains a peak value at $V_{\rm bg} \simeq 5.84$ V shown as the thick red line in the upper panel of Fig. 2(a). For $V_{\rm tg} \neq 0$, the double-peak feature emerges and results from the partial coverage of the top-gate region as mentioned earlier. It is then straightforward to express $R = R_e + R_{\rm ne}$, where $R_{e({\rm ne})}$ refers to the resistance contribution from the top-gate (non)effective region. As $V_{\rm tg}$ increases, the peak value of $R_e$ grows rapidly giving a nearly ninefold increase at $V_{\rm tg} = -8$ V and tends to grow further at higher $V_{\rm tg}$. $R_{\rm ne}$, on the other hand, shows relatively weak dependence on the $V_{\rm tg}$ and can be extracted unambiguously [orange dashed line in Fig. 2(a)]. The sheet resistance for the top-gate effective region $R_{\square e} = R_e W/L_e$, where $W$ is the width of BLG, can then be determined as shown in the upper panel of Fig. 2(b). At $V_{\rm tg} = 0$, the ratio $R_e/R \simeq 0.58$ is close to the length ratio of $L_e/L_s \simeq 0.59$ as expected [Fig. 1(a)].

The thick red curve in the lower panel of Fig. 2(a) shows the thermoelectric signal $V_s$ as a function of $V_{\rm bg}$ at $V_{\rm tg} = 0$. $V_s$ is nearly zero at the CNP and exhibits an ambipolar feature where electron-type ($V_s < 0$) and hole-type ($V_s > 0$) carriers can be readily tuned by $V_{\rm bg}$. It increases rapidly in magnitude with $V_{\rm bg}$ attaining local extremes and falls down at higher $V_{\rm bg}$. Similar to the analysis for resistance, we denoted $V_s = V_{\rm se} + V_{\rm sne}$, where $V_{\rm se(sne)}$ is the thermoelectric signal from the top-gate (non)effective region. When turning on $V_{\rm tg}$, $V_{\rm se}$ separates from the thick red curve with local extremes occurring at higher $V_{\rm bg}$ as $V_{\rm tg}$ increases in magnitude as shown in the lower panel of Fig. 2(a). The blue curves are $V_s$ signals at $V_{\rm tg} = \pm 10$ V that we used for the extraction of the $V_{\rm sne}$ shown as the dashed orange line in the lower panel of Fig. 2(b). However, the ratio of $V_{\rm se}/V_s \sim 0.37$ at $V_{\rm tg} = 0$ turns out to be about 20% less than the expected ratio of $L_e/L_s$ for a uniform $(-\nabla T)$ across BLG. This implies a smaller temperature gradient $(-\nabla T)_e$ under the top-gate effective region due to a likely heat shunt through the top-gate (Ti-Au)/hBN. By assuming that TEP at zero top-gate voltage is the same throughout the BLG, we can then determine $\Delta T_e$ and hence TEP $S_e = V_{\rm se}/\Delta T_e$ under the top-gate effective region shown in the lower panel of Fig. 2(b) [11]. At 15 K, the difference between local extremes $\Delta S_m$, defined in the inset of the lower panel in Fig. 2(b), equals 20 $\mu$V/K and is enhanced by more than fourfold to ~95 and 80 $\mu$V/K at $V_{\rm tg} = -7$ and 8 V, respectively.

The peak values $R_{\square e0}$ are plotted in log scale as a function of the corresponding $\vec{D}$ at different $T$ shown in Fig. 3(a). The solid symbols that extend to higher $\vec{D}$ are obtained from the same device after cooling down to the base temperature again, which shows consistent behavior. $R_{\square e0}$ increases exponentially with $|\vec{D}|$ giving $R_{\square e0} \simeq 230$ k$\Omega$ at $\vec{D} \simeq 1.2$ V/nm and 15 K, which is nearly a 40-fold increase compared to its value at zero $\vec{D}$. In order to gain further information on the band gap $E_g$, we plot the relative conductivity $R_{\square e0}(D = 0)/R_{\square e0}$ as a function of $100/T$ for eight different $\vec{D}$ values such that effects other than $\vec{D}$ can be excluded. The data points are then fitted in the temperature range of 50–300 K by using $R_{\square e0}(D = 0)/R_{\square e0} = A\exp(-E_g/2k_BT) + C$, where $A$ and $C$ are constants independent of $T$. The fitted curves are shown as red solid lines in Fig. 3(b), where the extrapolations to lower temperatures (dotted red lines) deviate slightly from the data points. The extracted $E_g$ vs $\vec{D}$ is shown in Fig. 3(c), which is practically linear for $\vec{D} \geq 0.3$ V/nm, giving a $E_g \simeq 100$ meV at $\vec{D} \simeq -0.9$ V/nm close to the value given by infrared microspectroscopy [7]. The data points show good agreement with the calculated band gap [solid line in Fig. 3(c)] using a self-consistent tight-binding model. The fitting function is based on a simplified model of a narrow band gap semiconductor with an impurity band that originates from disorder and impurity in BLG. The parameter $A$ reflects the $\vec{D}$ dependence of carrier mobility $\mu_c \equiv e\tau/m^*$. It turns out to increase with $|\vec{D}|$ [inset in

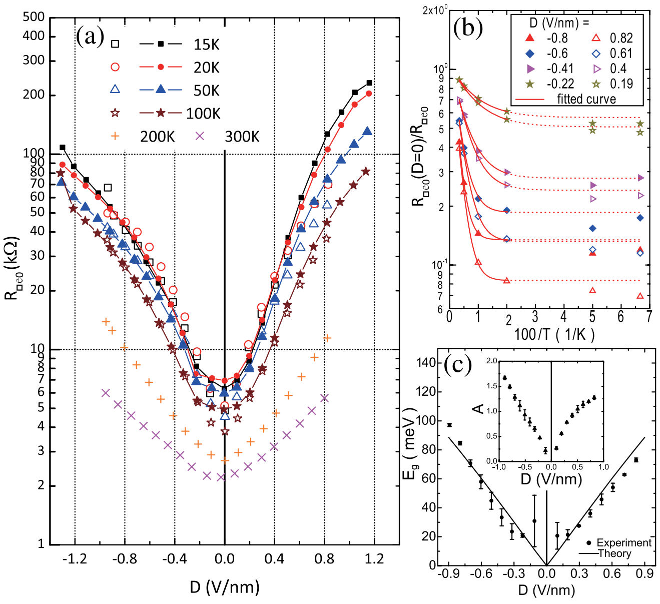

FIG. 3 (color online). (a) $R_{\square e0}$ (log-scale) vs $\vec{D}$ for the dual-gated BLG at 6 different temperatures ranging from 15 to 300 K. $R_{\square e0}$ exponentially grows with $\vec{D}$. (b) The relative conductivity $R_{\square e0}(D = 0)/R_{\square e0}(D)$ vs $100/T$ at 8 different $\vec{D}$ values. The red solid lines are the fitted curves in a temperature range of 50–300 K using $R_{\square e0}(D = 0)/R_{\square e0}(D) = A\exp(-E_g/2k_BT) + C$. The dotted red lines are extrapolations of the fitted curves to lower temperatures. The extracted band gap $E_g$ and $A$ parameter as a function of corresponding $\vec{D}$ are shown in (c). The solid line is the calculated band gap using the self-consistent tight-binding model.

Fig. 3(c)], where the charge redistribution (screening) and also change in band structure may play a role.

The relative increase of $S_m (\equiv \Delta S_m/2)$, i.e., $[S_m(D)/S_m(D=0)]-1$, is shown as open symbols in Fig. 4(a). $[S_m(D)/S_m(D=0)]-1$ grows larger at lower $T$ and exhibits a minor asymmetry with respect to $\vec{D}$. At 20 K, $[S_m(D)/S_m(D=0)]-1$ reaches a value of $\sim 4.2$ at $\vec{D} = 0.7$ V/nm. According to the Mott relation [15], we can deduce TEP from the sheet resistance data by using $S_e = \frac{\pi^2}{3}\frac{k_B^2}{e}[\frac{-T}{R_{\square e}}(\frac{\partial R_{\square e}}{\partial V_{\rm bg}})](\frac{\partial V_{\rm bg}}{\partial \varepsilon})_{\epsilon=\mu}$. The relative increase of the term $[\frac{-T}{R_{\square e}}(\frac{\partial R_{\square e}}{\partial V_{\rm bg}})]$ is shown as the solid lines in Fig. 4(a) without any scaling or shifting on them. For $T \leq 100$ K and $|\vec{D}| \leq 0.3$ V/nm, we find surprisingly good agreement in the solid lines to the measured values of $[S_m(D)/S_m(D=0)]-1$ (symbols). However, the solid lines start to deviate downward from the symbols as $|\vec{D}| \geq 0.4$ V/nm. Based on the Mott relation, the discrepancy should reflect the $\vec{D}$ dependence of the term $(dV_{\rm bg}/d\epsilon)|_{\epsilon=\mu}$ that is proportional to the density of states at $\mu$. We argue that, as $|\vec{D}|$ increases, more states near the CNP are pushed aside, forming a band gap that grows wider with $|\vec{D}|$. The density of states at band edges is then expected to increase with increasing $|\vec{D}|$. We also plotted the $\vec{D}$ dependence of $\Delta V_{\rm bg}$, defined in the inset in the lower panel in Fig. 2(b), and the corresponding carrier density $n_m$, where peak value $S_m$ occurs shown in the inset in Fig. 4(a). The gradual increase in $n_m$ at higher $|\vec{D}|$ is consistent with the scenario described earlier. However, for 200 and 300 K, the solid lines deviate upward instead. The failure of the Mott relation near the CNP at high $T$ is due to the violation for the criteria of $k_BT/\epsilon_F \ll 1$ ($\epsilon_F$ is the Fermi energy) as pointed out by several authors [14,16–18]. We note that the enhancement in TEP is mainly associated with the change in band curvature due to $\vec{D}$ rather than $n_m$ that shows relatively weak variation with $\vec{D}$ ($\leq 50\%$).

The $T$ dependence of $S_m$ at different $\vec{D}$ values is plotted in Fig. 4(b). It exhibits a maximum near 100 K, giving a value of $S_m(D = 0.7 \text{ V/nm}) \simeq 180\ \mu$V/K. Below 50 K, we remark that $S_m(\vec{D} = 0.7 \text{ V/nm})$ is comparable to the reported large TEP in sodium cobaltates $\text{Na}_x\text{CoO}_2$ ($x = 0.97$ and 0.88) [19] and $\text{Bi}_2\text{Te}_3$-based alloys ($\text{CsBi}_4\text{Te}_6$ [20] and $\text{Bi}_2\text{Te}_3$ [21]) shown as dotted lines. Unfortunately, the detailed information on thermal conductivity $\kappa$ in dual-gated BLG is absent for the determination of thermoelectric figure of merit $ZT \equiv S^2\sigma T/\kappa$, where $S$, $\sigma$, and $\kappa$ are TEP, electrical conductivity, and thermal conductivity, respectively [22]. Nevertheless, it was recently pointed out that $\kappa$ in encased few-layer graphene can be orders of magnitude smaller due to the quenching of the flexural phonon mode [23–25], which makes dual-gated BLG device a potential candidate for large $ZT$.

Theoretical calculations with a screening effect are based on Kubo's formula [12]. In the clean limit, the predicted relative increase of $S_m$ shown as dotted (15 K) and dashed (300 K) lines in Fig. 4(a) are more than threefold larger

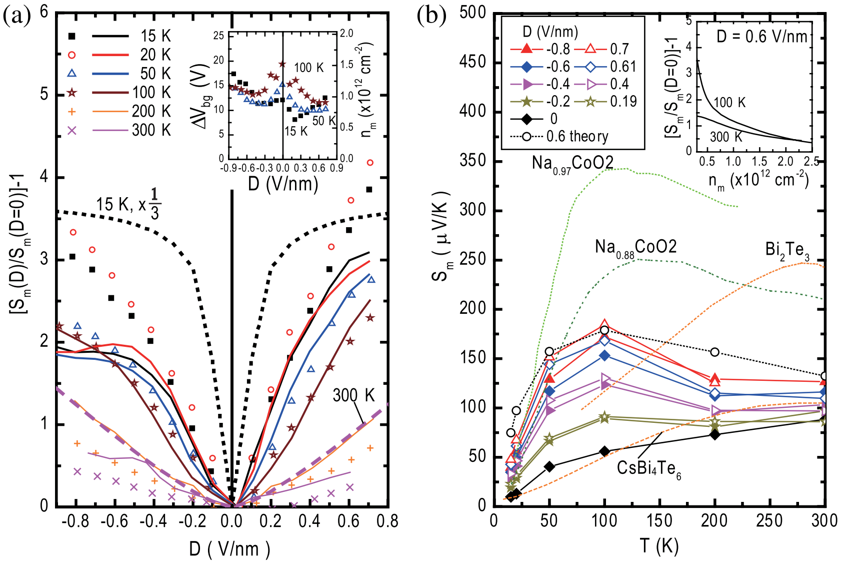

FIG. 4 (color online). (a) $[S_m(D)/S_m(D=0)]-1$ vs $\vec{D}$ for the dual-gated BLG at 6 different temperatures ranging from 15 to 300 K. The solid lines are the relative increase of $[\frac{-T}{R_{\square e}}(\frac{\partial R_{\square e}}{\partial V_{\rm bg}})]$ obtained from the $R_{\square e}$ data. The dotted and dashed lines are the theoretical prediction at 15 and 300 K, respectively. The 15 K dotted line is scaled by 1/3 for clarity. The inset figure plots $\Delta V_{\rm bg}$ and its corresponding carrier density $n_m$ at which $S_m$ occurs as a function of $\vec{D}$. (b) $T$ dependence of $S_m$ for the dual-gated BLG at 9 different $\vec{D}$ values ranging from $-0.8$ to 0.7 V/nm are shown as symbols. The dotted line with an open circle derives from the theoretical calculation using experimental $n_m$ values. The TEP values for $\text{Na}_x\text{CoO}_2$ ($x = 0.97$ and $x = 0.88$), $\text{Bi}_2\text{Te}_3$, and $\text{CsBi}_4\text{Te}_6$ are shown as dotted lines for comparison. The inset figure shows the theoretical calculation of $[S_m(D = 0.6 \text{ V/nm})/S_m(D=0)]-1$ vs $n_m$.

than our experimental results. The corresponding $n_m$, however, is an order of magnitude smaller. The excess charges near the CNP in our device likely originate from electron-hole puddles, which is reminiscent of the finite minimum conductivity [26–29], caused by charge impurities with a density of $n_i \approx 4 \times 10^{11}\ \mathrm{cm}^{-2}$ estimated from the CNP position $V_{\mathrm{bg0}} = 5.84\ \mathrm{V}$ [30–32]. Based on the self-consistent theory [29,33], we further obtain the corresponding potential fluctuation amplitude $\delta V \approx n^* \frac{\pi \hbar^2}{2m^*} \approx 160\ \mathrm{K}$ in our device, where $n^* = \sqrt{n_i}/\xi^2 \simeq 6 \times 10^{11}\ \mathrm{cm}^{-2}$ is the residual density due to charge puddles of size $\xi \simeq 10\ \mathrm{nm}$ [26,32]. In a gapped BLG, the potential fluctuation creates impurity states near the band edges. We remark that $\delta V$ sets an important energy scale above which the carriers associated with electron-hole puddles are delocalized, forming an impurity band. This explains the good $E_g$ fitting [Fig. 3(b)] and also the nearly $1/T$ dependence of $S_m$ [Fig. 4(b)] as expected for a degenerate semiconductor at high $T$ ($T \gtrsim \delta V$). For $T \lesssim \delta V$, the impurity states become more localized while dominating the charge transport through nearest neighbor hopping. By considering a simplified two-band model with electron-type and hole-type carriers near the CNP [18], the compensated TEP can be expressed as $S = S'(|n_h| - |n_e|)/(|n_h| + |n_e|)$, where we have assumed the same TEP magnitude $S'$ and mobility for each band and $n_{e(h)}$ is the electron (hole) density. At the CNP, $S = 0$ and then both $|n_e|$ and $|n_h|$ equal half of $|n^*|$. We, therefore, expect $S_m$ to occur at $|n_m| \approx |n^*/2| \simeq 3 \times 10^{11}\ \mathrm{cm}^{-2}$ such that either $n_e$ or $n_h$ is vanishing. This turns out to be reasonably close to the $n_m$ values ($\approx 5\text{–}15 \times 10^{11}\ \mathrm{cm}^{-2}$) in our device. We emphasize that $[S_m/S_m(D = 0)] - 1$ depends critically on $n_m$ as shown in the inset in Fig. 4(b) obtained from the theoretical calculation for $\vec{D} = 0.6\ \mathrm{V/nm}$. If using the experimental values of $n_m$, the calculated $S_m(\vec{D} = 0.6\ \mathrm{V/nm})$ [open circles in Fig. 4(b)] gives much better quantitative agreement with the experimental data. However, more rigorous TEP calculation is needed to incorporate the electron-hole puddle effect in a gapped BLG.

In conclusion, we demonstrate the electric-field tunable band gap and TEP in a dual-gated BLG device, which may offer a new platform for innovative science and engineering. Unfortunately, excess charges due to charge puddles near the CNP greatly reduce the enhancement of TEP. It gives $S_m(15\ \mathrm{K}, D = 0.7\ \mathrm{V/nm}) = 48\ \mu\mathrm{V/K}$ that is already comparable to or exceeding existing records for low-$T$ thermoelectric materials. Larger enhancement, in principle, can be realized in a cleaner dual-gated BLG device at higher $\vec{D}$. With the advantage of full electric-field control on TEP and also its carrier polarity, dual-gated BLG device with a proper design can be a promising candidate for low-$T$ thermoelectric application.

The authors thank C. R. Chang, H. T. Jeng, and W. C. Lee for fruitful discussions. We acknowledge the funding support from National Science Council in Taiwan (NSC99-2112-M-001-032-MY3) and technical support from Core Facility for Nanoscience and Nanotechnology at Academia Sinica in Taiwan.

---

*wlee@phys.sinica.edu.tw

[1] E. McCann and V. I. Fal'ko, Phys. Rev. Lett. **96**, 086805 (2006).
[2] J. Martin *et al.*, Phys. Rev. Lett. **105**, 256806 (2010).
[3] Y. Barlas, R. Côté, J. Lambert, and A. H. MacDonald, Phys. Rev. Lett. **104**, 096802 (2010).
[4] T. Ohta *et al.*, Science **313**, 951 (2006).
[5] E. V. Castro *et al.*, Phys. Rev. Lett. **99**, 216802 (2007)
[6] J. B. Oostinga *et al.*, Nature Mater. **7**, 151 (2007).
[7] Y. Zhang *et al.*, Nature (London) **459**, 820 (2009).
[8] H. Miyazaki *et al.*, Nano Lett. **10**, 3888 (2010).
[9] T. Taychatanapat and P. Jarillo-Herrero, Phys. Rev. Lett. **105**, 166601 (2010).
[10] C. R. Dean *et al.*, Nature Nanotech. **5**, 722 (2010).
[11] See Supplemental Material at http://link.aps.org/supplemental/10.1103/PhysRevLett.107.186602 for details of device fabrication and the measurement method.
[12] L. Hao and T. K. Lee, Phys. Rev. B **81**, 165445 (2010); **82**, 245415 (2010).
[13] J. P. Small, K. M. Perez, and P. Kim, Phys. Rev. Lett. **91**, 256801 (2003).
[14] C. R. Wang, W. S. Lu, and W. L. Lee, Phys. Rev. B **82**, 121406(R) (2010).
[15] M. Cutler and N. F. Mott, Phys. Rev. **181**, 1336 (1969).
[16] S. G. Nam, D. K. Ki, and H. J. Lee, Phys. Rev. B **82**, 245416 (2010).
[17] D. Wang and J. Shi, Phys. Rev. B **83**, 113403 (2011).
[18] E. H. Hwang, E. Rossi, and S. Das Sarma, Phys. Rev. B **80**, 235415 (2009).
[19] M. Lee *et al.*, Nature Mater. **5**, 537 (2006).
[20] D. Y. Chung *et al.*, Science **287**, 1024 (2000).
[21] L. R. Testardi, J. N. Bierly, Jr., and F. J. Donahoe, J. Phys. Chem. Solids **23**, 1209 (1962).
[22] G. J. Snyder and E. S. Toberer, Nature Mater. **7**, 105 (2008).
[23] J. H. Seol *et al.*, Science **328**, 213 (2010).
[24] L. Lindsay, D. A. Broido, and N. Mingo, Phys. Rev. B **82**, 115427 (2010).
[25] W. Jang *et al.*, Nano Lett. **10**, 3909 (2010).
[26] W. Zhu, V. Perebeinos, M. Freitag, and P. Avouris, Phys. Rev. B **80**, 235402 (2009).
[27] Y. W. Tan *et al.*, Phys. Rev. Lett. **99**, 246803 (2007).
[28] S. Das Sarma, E. H. Hwang, and E. Rossi, Phys. Rev. B **81**, 161407(R) (2010).
[29] S. Xiao *et al.*, Phys. Rev. B **82**, 041406(R) (2010).
[30] J. Martin *et al.*, Nature Phys. **4**, 144 (2007).
[31] Y. Zhang *et al.*, Nature Phys. **5**, 722 (2009).
[32] A. Deshpande *et al.*, Appl. Phys. Lett. **95**, 243502 (2009).
[33] S. Adam *et al.*, Proc. Natl. Acad. Sci. U.S.A. **104**, 18 392 (2007).